Numerical and experimental analysis of the power output performance of a point absorber WEC for nearshore wave conditions

Jonathan Everett [a,*], Vladislav Sorokin [a], Colin Whittaker [b], Kean Aw [a]

[a] Department of Mechanical and Mechatronics Engineering, The University of Auckland, New Zealand
[b] Department of Civil and Environmental Engineering, The University of Auckland, New Zealand

ARTICLE INFO

ABSTRACT

A single-degree-of-freedom Wave Energy Converter (WEC) that harvests energy from heave and surge motion of waves in nearshore conditions has been designed. The device targets supplying energy to aquafarms and attaches to an existing structure. The device consists of a buoy that slides up and down with waves along a linear rail, with this linear motion converted into the high-frequency rotation of a generator using magnetic coupling. The effects of mounting orientation (angle of linear rail to the vertical) of the device on the power output were studied for a range of wave parameters. A scale model was manufactured and tested in a wave flume, using mono-frequency waves in intermediate water depths. The study reveals that increasing the mounting orientation angle enhances power output across all tested frequencies. The results show a power increase of up to 50% with a 45-degree mounting angle compared to 0 degrees, with an average increase of 35% across the considered frequencies. Time-domain modelling in Simulink complements the experimental investigations, providing similar results to the experimental study. In summary, this study demonstrates the efficacy of the designed single-degree-of-freedom WEC for energy harvesting in nearshore conditions, emphasising the critical role of mounting orientation in maximising power generation.

1. Introduction

There is a very large ocean wave energy resource with the potential to provide renewable energy. Approximately 70% of the earth's surface is covered in water, most of which consists of oceans. The energy density of waves is significantly higher than other renewable energy sources, such as solar and wind energy. Ocean waves have an energy density of 2 to 3 kW/m^2, compared to 0.4–0.6 kW/m^2 for wind and 0.1–0.2 kW/m^2 for solar (Lopez et al., 2013). There are other advantages to wave energy besides high energy density. The energy densities of ocean waves tend to be more consistent (albeit under varying wave conditions) than wind or solar and are straightforward to predict. Also, generation is not confined to daylight hours like solar energy. Wave energy, of course, also has its challenges. The two most significant issues are the economic viability and survivability of devices in ocean conditions. Devices must be designed to survive extreme weather events, such as cyclones, and resist saltwater corrosion and biofouling. Designing against these obstacles typically results in high costs of development and manufacture, making the device less likely to be commercially viable.

Numerous wave energy devices exist across a range of operating principles, scales and ocean conditions, including those proposed recently (Li and Jing, 2021; Cai et al., 2022; Jiang et al., 2020). Although slightly reductive, most WECs can be characterised into one of three categories: oscillating body systems (OBS) (CorPower, 2023; Ocean Power Technologies, 2024; Swel, 2024; TETHYS, 2020; Salter, 1980; Pecher et al., 2012), overtopping devices (TETHYS, 2018), and oscillating water columns (OWC) (WaveSwell, 2023). There are many ways to assess these devices, such as levelised cost of energy (LCOE), capture width ratio (CWR) and the power-to-mass ratio of the device (Ermakov and Ringwood, 2021; CorPower, 2023). Although not the most advanced metric, the power-to-mass ratio can be used to get an approximate idea of how the device is performing. Leading WEC developers CorPower, WaveSwel and Wello each provide power generation projections based on modelling and ocean deployment of scale prototypes. The Wello Penguin deployed a 1600-tonne full-scale prototype, which generated a maximum of 700 kW (0.44 W/kg), with continuous power production of 160–180 kW (0.1–0.11 W/kg) (TETHYS, 2020). CorPower have predicted a yearly power production of 10 MWh/tonne, or 1.14 W/kg of continuous power (CorPower, 2023), for their 70-tonne device. Swel's Waveline Magnet generated a peak of 1.4 kW at 1800 kg (0.78 W/kg) in a large-scale wave flume experiment (Steffen, 2022).

---

* Corresponding author.
 E-mail address: jeve608@aucklanduni.ac.nz (J. Everett).

Symbols

θ	WEC mounting angle
Z_{buoy}	Buoy wave following amplitude
z'	Buoy displacement along linear rail
H	Wave height
λ	Wavelength
F_h	Heave force
F_s	Surge force
β	Instantaneous wave slope
F_{PTO}	PTO force
K_{PTO}	PTO damping coefficient
F_{fr}	Friction force
F_m	Mooring force
F_{rad}	Vertical radiation force
F_w	Weight force
m	Mass of the buoy
g	Acceleration due to gravity
η	Free surface elevation of the wave
ρ	Fluid density
a	Added mass coefficient in the vertical axis
b	Added damping coefficient in the vertical axis
C_a	Added mass coefficient in the horizontal axis
C_D	Viscous damping coefficient in the horizontal axis
u	Horizontal fluid velocity
w	Vertical fluid velocity
x	Horizontal buoy position
z	Vertical buoy position
P_{RMS}	Root mean squared (RMS) power
V_i	Instantaneous voltage
R	Resistance
C_{vel}	Velocity factor

Wave energy technology has seen numerous prototypes developed and commercial attempts made, yet scaling these solutions to meet large-scale energy demands remains challenging. An alternative approach is to explore niche applications for wave energy devices, particularly in fast-growing marine industries such as aquaculture. The aquaculture industry is a rapidly growing sector with changing energy demands, typically met by costly diesel generators with minimal use of renewable energy sources. This reliance on diesel results in significant expenses and contributes to greenhouse gas emissions. The energy requirements of aquafarms can vary widely, ranging from less than 4 MWh/year for small mussel farms to over 700 MWh/year for larger fish farms (USDOE, 2019). This spectrum of energy needs presents an opportunity to deploy smaller-scale WECs tailored to specific applications within aquafarming.

A recent study explored the feasibility of different wave energy converters to supply power to aquafarms at two sites in Portugal, making a positive case for the integration of wave energy into the aquaculture industry (Clemente et al., 2023). Numerous similar studies have been done for other locations (Yue et al., 2023; Freeman et al., 2022). While certain aquafarms have significant energy demands requiring large-scale solutions, many small-scale operations on aquafarms, such as water purification systems (200 W) or aerators(100 W) (USDOE, 2019), could benefit from smaller WECs.

Aquaculture operations typically occur in sheltered bays and harbours. In these locations, wave energy resources are smaller, but wave direction is more consistent and extreme weather conditions are less prevalent. Small-scale WECs optimised for these conditions have significant potential. Even a modest power output from a WEC could prove valuable for supporting essential operations on small aquafarms, offering a sustainable alternative to diesel generators and contributing to the broader transition towards renewable energy solutions in aquaculture.

The present paper details the development and theoretical and experimental study of a single-degree-of-freedom point absorber WEC that can harvest energy from the combined heave and surge motions of the waves. The WEC is designed to operate in nearshore wave conditions and targets supplying electricity to aquafarms. A scale model has been manufactured and then tested in idealised conditions similar to what is typical for New Zealand aquafarms. The impact of surge wave motion on the performance of the device is investigated experimentally and numerically.

The WEC consists of a buoy that can slide up and down with waves along a linear rail, with this linear motion converted into the high-frequency rotation of a generator using magnetic coupling. Various linear to rotational mechanisms have been used in other WECs, e.g. CorPower uses a rack and pinion style mechanism to convert the linear motion to rotational (CorPower, 2023), whilst InfinityWEC (Ocean Harvesting, 2023) uses a dual ball-screw mechanism. These, as well as most other WECs, are designed to operate in deep water conditions. Nearshore use of WECs is less common than offshore because the gross wave energy is typically much lower when compared to deep water (Folley and Whittaker, 2009). Folley and Whittaker have used a spectral wave model to assess nearshore wave energy resources and showed that while the gross wave energy present is significantly decreased, the exploitable energy does not decrease significantly (a decrease of 7% and 22% for the two sites studied). Folley et al. (2007) experimentally showed that a small surging WEC performs better when close to shore, primarily because the surge motion of the waves is enlarged in shallow water (Brown, 2016). Folley et al. (2007) also found that the power generation of the top hinged flap-type WEC was more related to the incident wave force than the incident wave power. Negri and Malavasi (2022) have developed a heave and surge device which is experimentally analysed in nearshore conditions. The design consists of a float that heaves to rotate a lever arm, with a perpendicular lever branching off the main lever that is moved by the surge motion of the wave. It was concluded that the energy available in the surge direction increased until the breaking point and that adding an additional degree of freedom in the surge direction did not significantly impact the power available in the heave direction. Work on a WEC design by Evans et al. (1979) demonstrates theoretically that the power capture in small waves can approach 100% when at least two modes of energy capture are used, in his case heave and surge. When constrained to only one mode, the captured power is limited to 50%. The device consists of a submerged circular cylinder that is constrained by springs and dampers to make tuneable oscillations. From this work, it is known that capturing both the heave and surge motion of the waves can result in significant increases in power generation. Thus, the WEC proposed in the present paper is designed to capture both heave and surge motion of the waves.

The paper is structured as follows. Section 2 outlines the concept of the device and its operating principle. Section 3.1 presents governing equations used for modelling the device dynamics that were implemented in the theoretical model to predict the WEC performance. Section 3.2 outlines the manufacturing and experimental procedures for the WEC model used for testing it at the wave flume. Section 4 presents the results of the theoretical and experimental analysis of the WEC performance; a discussion of the effects of the wave conditions and device parameters on the power output is provided. Section 5 outlines the main conclusions of the paper. Finally, Section 6 discusses possible areas of future work.
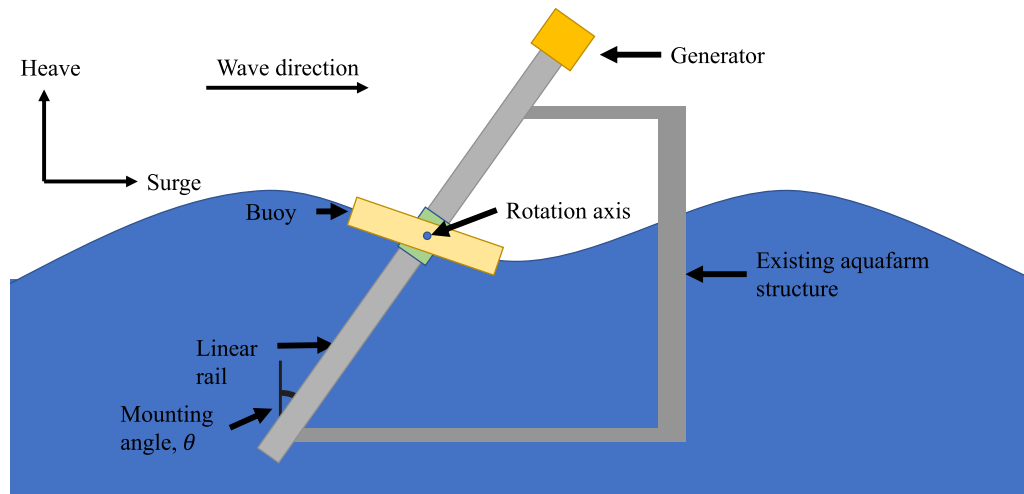
Fig. 1. Schematic of the WEC concept.

2. Concept

A schematic diagram of the wave energy converter is shown in Fig. 1. The WEC can be classified as a point absorber device, a type of oscillating body device, meaning that its dimensions are small relative to the length of the incident waves. The WEC is designed to attach to an existing aquafarming structure, aligned to face the dominant wave direction. The structure is floating and moored or large enough to resist the motion of the waves, as is typical for aquafarming structures (The New Zealand Government, 2019). The resistance to motion of an aquafarming structure has been shown experimentally (Stevens et al., 2007). Stevens et al. recorded accelerometer data of a mussel farm long-line undergoing wave excitation; at two floating points, displacement heights of 0.1 to 0.5 m were measured in waves of 1.5 m in height.

The buoy slides up and down with the waves along a linear rail and is magnetically coupled to a mechanism inside the rail, which converts the linear motion to rotational motion, driving a generator. The buoy is able to freely pitch along the rotation axis indicated in Fig. 1. This allows it to smoothly follow the surface of the incident waves.

The shape of the buoy was selected to maximise the restoring "spring" coefficient of heave motion (Eq. (4)), as the device is designed to be a wave following WEC. Consider a buoy with a lower cross-sectional area and, therefore, a lower restoring spring coefficient of heave motion. The change in buoy submersion required to overcome a unit force will be higher, which applies to fixed forces such as friction. A lower effective spring coefficient essentially reduces the effective amplitude of the wave, as some height is lost in overcoming the fixed forces. Since this WEC is for use on an aquafarm, where waves are typically small, a higher width-to-height ratio was selected. It is acknowledged that the geometry of the buoy can have a large impact on power output. For example, a complex geometry resulting in larger drag forces could be beneficial, but detailed optimisation of the buoy geometry is outside the scope of this work.

The mounting angle of the WEC (the angle between the linear rail and the vertical) can also be customised to maximise the power output. This mounting angle is the main parameter investigated in this study.

The concept is partly based on the hypothesis that increasing the device's mounting angle, θ, will increase the power output, particularly in shallow and intermediate water depths, where the surge component of wave motion is larger than the heave. There is one core reason behind this hypothesis. In a scenario where the buoy is following the wave, at a larger angle the buoy moves further and faster, as it will have the same component of heave motion regardless of the angle. The wave

following amplitude of buoy motion is therefore given by the following:

$$Z_{buoy} = \frac{H}{2\cos(\theta)} \tag{1}$$

where H is the wave height and θ is the WEC mounting angle. A similar equation for the wave following amplitude has been used in Yurchenko and Alevras (2018) for a linearly moving WEC consisting of a buoy with a pendulum power take-off (PTO). While this reasoning is quite simplified, and for example does not fully account for the surge motions, it can still illustrate the potential of increasing the mounting angle from zero to increase the WEC power output.

3. Numerical and experimental analysis

3.1. Governing equations and numerical modelling

There are numerous ways in which a WEC can be numerically modelled, with varying complexity. Choosing a method is typically a tradeoff between computational expense and accuracy. In this paper, the Matlab software Simulink was used to model the WEC as a single-degree-of-freedom (SDOF) system in the time domain. Although there are several available software packages for WEC modelling, we developed our own model, as the non-complex geometry of our WEC would allow a computationally inexpensive Simulink model to be used without sacrificing accuracy. It also provided us with the flexibility to quickly change parameters to assess the WEC performance under different wave conditions.

The fact that the buoy can rotate around the pitch axis adds a second degree of freedom into the system. However, the buoy rotates freely and aligns closely with the slope of the wave. Thus, this rotation was approximately modelled via a buoyancy force normal to the wave slope, allowing a SDOF system to be used in the Simulink modelling of the WEC behaviour.

An experimental study by Giassi et al. demonstrates that simplified numerical models work well to describe the dynamics of PTO and power absorption for point absorber WECs, in both regular and irregular waves (Giassi et al., 2020). The research showed that the qualitative behaviour of power absorption is well predicted by both frequency and time domain models. The simplified method is accurate so long as no instabilities occur, i.e. instabilities due to resonance. Since the proposed concept does not utilise resonance and does not have the potential for instabilities of this nature, a simplified SDOF model can be used. It should be noted that although the system is modelled as SDOF, several
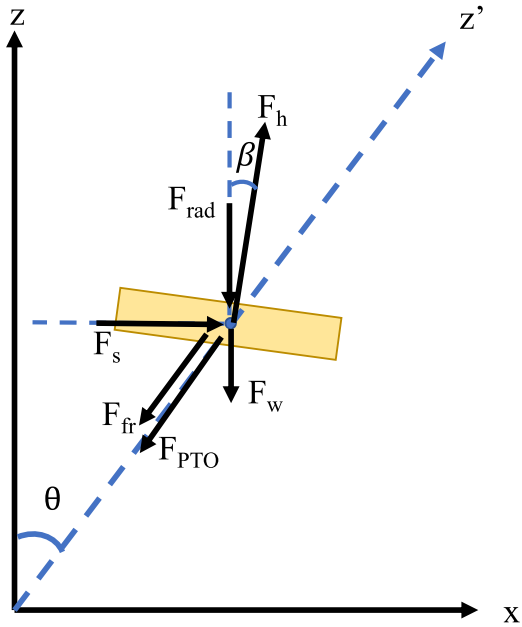
Fig. 2. Diagram of forces and rotated coordinate system.

of the forces do not align with the direction of this degree of freedom and instead must be projected onto it.

The equation of motion used to model the proposed WEC is as follows:

$$m\ddot{z}' = F_h \cos(\theta - \beta) + F_s \sin(\theta) + F_{PTO} + F_{fr} + F_m + F_{rad} \cos(\theta) - F_w \cos(\theta)$$
(2)

where m is the mass of the buoy, z' is the buoy displacement along the linear rail, F_h is the heave force due to buoyancy, F_s is the horizontal surge force, F_{PTO} is the power take-off force, F_{fr} is the parasitic friction force, F_m is the mooring force, F_w is the weight force, and F_{rad} is the vertical radiation force modelled using hydrodynamic coefficients, added mass and damping. The power take-off force is considered linear damping, with the force directly proportional to the buoy velocity. A free-body diagram of this system is shown in Fig. 2. The axis z' corresponds to the linear rail the buoy is constrained to move along, θ is the device mounting angle, and β is the instantaneous wave slope. The mooring force acting in the z' direction will be zero, so it is neglected from the diagram. There is no mooring force opposing the linear motion of the buoy as the motion is constrained to one axis, and the linear rail is mounted rigidly to an existing structure and is assumed to have no motion. The friction force F_{fr} is a force of constant magnitude that acts in the opposite direction of buoy motion. The weight force is given as follows:

$$F_w = mg$$
(3)

where m is the buoy mass and g is the acceleration due to gravity.

The wave excitation forces (F_h and F_s) are produced by incident waves on the buoy. The heave force, F_h, occurs due to buoyancy and acts normal to the wave slope. This is a feature of the freely rotating buoy, as the buoy will always be at an approximate tangent to the wave slope. The heave force is defined by Eq. (4).

$$F_h = c(\eta - z)$$
(4)

where η is the free surface elevation of the wave, z is the vertical buoy displacement from the undisturbed equilibrium position, and c is the restoring "spring" coefficient defined by:

$$c = \rho g A_w$$
(5)

where ρ is the fluid density, and A_w is the water plane area of the buoy, assuming the buoy has a constant cross-sectional area along its height. Numerous available wave theories can be used to model the free surface elevation η and other wave properties, and the most suitable model depends on the wave conditions. Different wave theories have been used in the developed numerical model, depending on specific wave conditions measured in the experiments. The theories include the 3rd-order Stokes wave theory and the 5th-order Stream function. Elaboration on this can be found in Section 3.3.

In practice, the heave force can be obtained by integrating the pressure over the submerged area of the buoy. If the buoy has a flat bottom and is parallel to the free surface, then the pressure distribution across the bottom will be approximately uniform, and the force can be expressed simply as the average pressure multiplied by the area.

The PTO force is calculated based on the following equation:

$$F_{PTO} = \dot{z}' K_{PTO}$$
(6)

where K_{PTO} is the PTO damping coefficient. Consequently, the simulated power output at each instance in time is given by:

$$P_{out} = \dot{z}' F_{PTO}$$
(7)

The added damping and added mass coefficients can be used to model the fluid–structure interactions due to wave radiation (Hamilton, 2016). When the buoy moves vertically in water, it will generate waves that radiate from it, decreasing the buoy's kinetic energy. This effect is modelled by the added damping coefficient. Additionally, some water particles will move with the buoy when moving, effectively resulting in additional mass. This results in the vertical radiating force term as follows:

$$F_{rad} = -b\dot{z} - a\ddot{z}$$
(8)

where b is the added damping coefficient and a is the added mass coefficient.

Due to the constrained nature of the WEC concept (the buoy only moves along one axis), there will be significant relative velocities between the buoy and surrounding fluid, particularly in the horizontal direction. As a result, the surge force F_s occurs due to viscous drag. Morison elements are used to model this force (WEC-sim, 2022), defined by:

$$F_s = \rho V C_a(\dot{u} - \ddot{x}) + C_D(u - \dot{x})|u - \dot{x}|$$
(9)

where C_a is the horizontal added mass coefficient, C_D is the viscous drag coefficient, u is the horizontal fluid velocity, V is the submerged volume, ρ is the fluid density and $\dot{x}$ is the horizontal buoy velocity. Under normal operating conditions, the relative velocity between the wave and buoy in the vertical direction is much lower than in the horizontal direction. Experimental results discussed in Section 4.3 combined with analysis of wave theory solutions indicate that the relative velocity between the water particles and the buoy is more than three times higher in the horizontal direction than the vertical, even when PTO damping coefficients are very high. At lower PTO damping, the vertical relative velocity is even smaller. This is because motion in the vertical direction is mostly in phase, while horizontal motion is approximately 90 degrees out of phase. Also, horizontal wave velocity is greater than the vertical in shallow and intermediate depth waves. Due to the low magnitude of vertical relative velocity, the effects of nonlinearities in the vertical direction are assumed to be negligible.

The hydrodynamic and drag coefficients depend on the submerged object size, geometry and the relative velocities. These coefficients are tabulated for simple geometries, e.g. in Newman (1977) and Hamilton (2016), while for more complex geometries, they can be calculated numerically. Other structural components of the WEC itself will also affect the dynamics of the moving buoy. Consider the linear rail component of the WEC design. At nonzero angles, waves will reflect off the rail to assist the buoy in travelling along the rail. This could result in differing hydrodynamic and drag coefficients for different mounting angles.
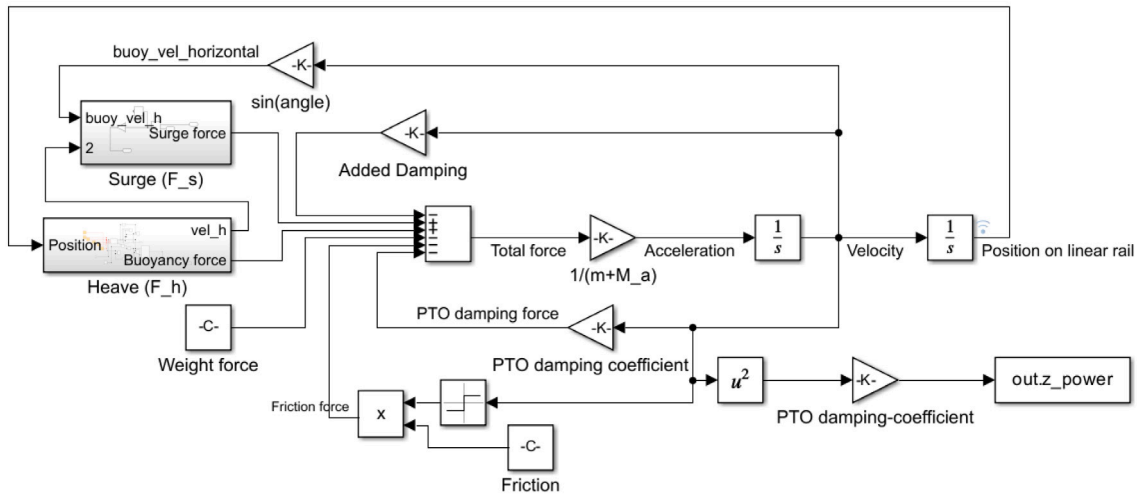
Fig. 3. Simulink model of the system.

There are several hydrodynamic coefficients that need to be considered in the numerical model, including a coefficient for viscous drag in the surge direction. The hydrodynamic coefficients were calculated for both the heave and surge direction, with the resulting forces projected onto the axis of buoy motion. To obtain the hydrodynamic coefficients, the following process was used. The CAD model of the buoy was imported into a hydrodynamic diffraction model in ANSYS AQWA, which utilises the boundary element method (BEM) to obtain solutions. The system conditions were input into the model, such as wave conditions, the physical properties of the buoy, and the water depth. Frequency-dependent values for the added mass and added damping were obtained for the heave axis, as was the added mass in the surge axis.

However, the viscous drag coefficients were not immediately available from this particular model, so an additional method was needed. Viscous drag coefficients in external flow are tabulated for simple geometries, with Reynolds number conditions given. For more complex geometries, the drag coefficient can be obtained via CFD modelling. For the buoy of this WEC, the geometry is complicated enough to justify using CFD, which was done using ANSYS CFX solver. The CFX model was first used on an object with a known drag coefficient (a cube) to validate it, followed by the buoy geometry. It is acknowledged that there are some limitations in the methods used to obtain these coefficients, particularly the viscous drag coefficient. The drag coefficient was obtained assuming a constant external flow, when in reality the fluid velocity is oscillating. The wetted area of the buoy will also change with the wave oscillations, resulting in a varying drag coefficient value. It has been assumed that the drag coefficient can be represented by a fixed value in this numerical study.

The Simulink model was built to reflect Eq. (2), and the necessary parameters and coefficients were provided in a Matlab script. The hydrodynamic coefficients from the ANSYS analysis were input into the Matlab script. The coefficients were obtained for a range of wave parameters, to match the experimental conditions. The script calls the Simulink model for a range of parameters, returning the power output and physical response to the wave excitation.

Fig. 3 shows a block diagram of the model. As previously discussed in this section, the model was implemented to reflect the concept, including all forces from Eq. (2). Arrays of wave heights and velocities were computed using the relevant wave theories and were input into the Simulink model. Each term from Eq. (2) is included in the Simulink model, with the exception of F_m, which has been defined as zero. The figure shows two subsystems, "Surge" and "Heave", which represent F_s in Eq. (9) and F_h in Eq. (4) respectively.

3.2. Experimental study

3.2.1. Scale model

To get experimental data on the performance of the WEC, a scale model was fabricated and tested in the wave flume at the University of Auckland. The model is shown in Fig. 4(a). The model works as described in Section 2, with the buoy moving up and down the 2.0 m long aluminium square extrusion to drive a generator. Fig. 4 shows the mechanism that allows this to work. The 6.4 kg buoy is magnetically coupled to a carriage inside the square tube, which moves with the buoy. The carriage is connected to a helix with wheels. The helix is constrained to only rotate, so it is forced to spin as the carriage moves up and down. Both the buoy and internal carriage roll along the square tube with wheels to minimise the friction of the mechanism. The WEC model is approximately 1:4 scale of the full-scale device.

The mounting of the buoy to the shaft can be seen in Fig. 4(a). The external carriage rolls along the shaft on 16 wheels and is magnetically coupled to a complimentary carriage inside the square tube. The buoy is then attached to the external carriage by one singular axis, which allows it to pivot to follow the surface of the incident waves better. The buoy comprises of a frame from aluminium extrusion profiles, with non-porous foam blocks attached beneath it for buoyancy.

A waterproof seal was required at the bottom of the aluminium square tube, as this end is submerged in water. This was achieved by manufacturing a flange to attach to the bottom. This flange was laser cut from several pieces of acrylic, which was then glued to the square tube and sealed with silicone. A rubber gasket was clamped over the flange with a final piece of acrylic. This seal can be seen in Fig. 4(d). This figure also shows the attached feet, which provide a means to constrain the bottom of the model. The angle of the feet can be easily adjusted to suit the mounting angle.

3.2.2. Experiment setup

The testing was completed in the wave flume at The University of Auckland's Fluid Mechanics Laboratory. The wave flume is 17 m long, 1.2 m wide and 1.8 m deep, with a water depth of 0.82 m being used for the testing. The flume uses a piston-type wave-maker, and there is a perforated parabolic beach at the opposite end for wave dissipation and reflection mitigation, although there is no active wave absorption. Two wave gauges were used in the experiment, approximately one metre before and after the device, located on the centreline of the flume. The wave gauges used are Edinburgh Designs WG8USB, which measure the free surface elevation via resistance between two partially submerged probes with a sample frequency of 128 Hz. The gauges have a measurement error of less than 0.1% when used at full scale.
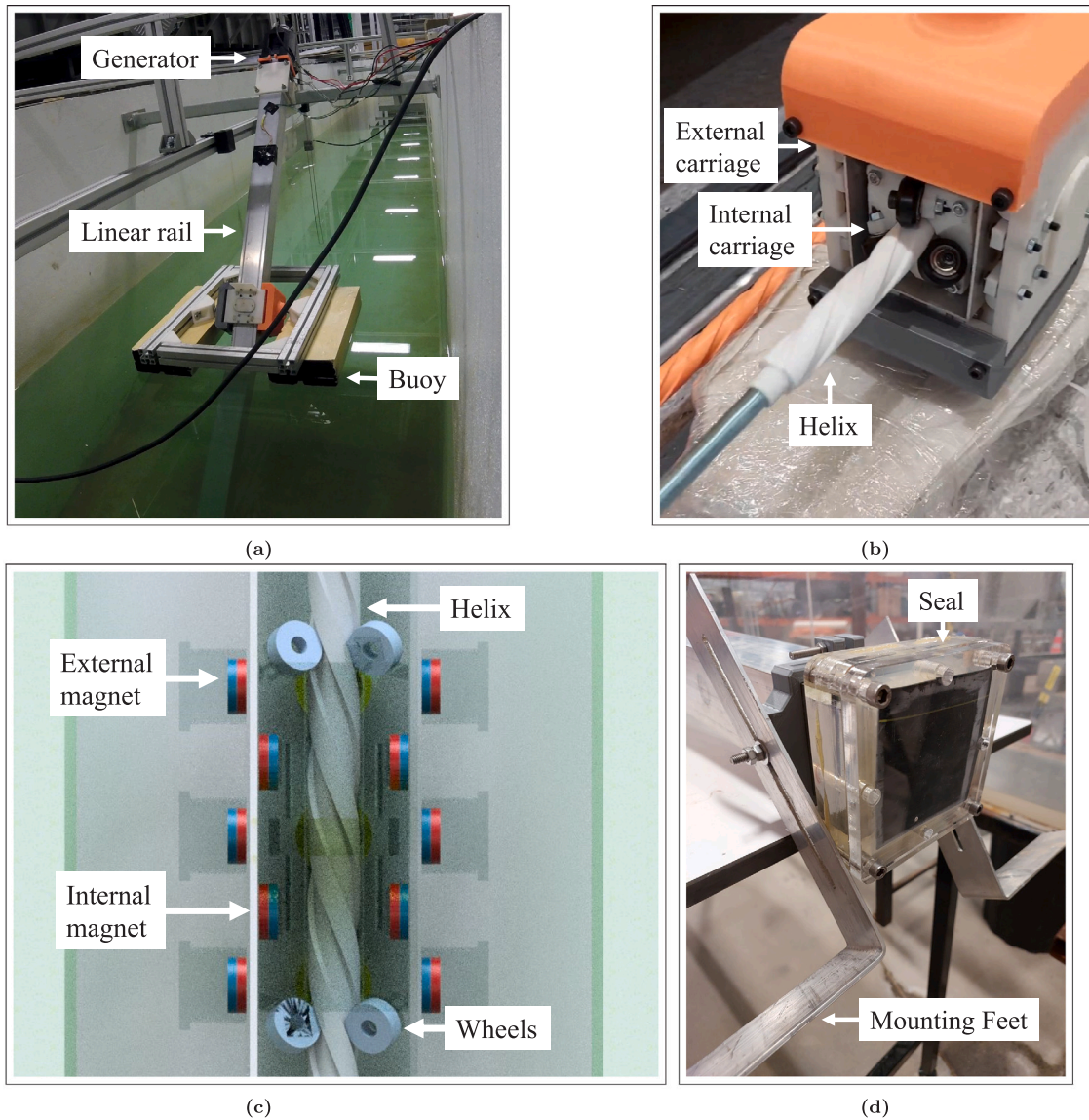
Fig. 4. Images of the WEC model: (a) WEC model in the wave flume; (b) linear to rotational mechanism; (c) drawing of mechanism; (d) waterproof seal.

Fig. 5 shows a diagram of the experimental setup. The WEC model was mounted to a rigid crossbar 9 m from the wave-maker and 0.5 m from the side. It was mounted by clamping it to the steel crossbar structure and by holding the device to the flume bed with lead weights on the adjustable feet. This leaves the buoy free to move when excited by the incident waves. Unlike the conceptual design, the model is mounted to the bed instead of solely to a large floating body. A limitation of the experimental setup is that the motion of the large floating body is not considered. It has been assumed that the floating body is sufficiently large to resist the motion of the waves and will not undergo any significant motion of its own (Stevens et al., 2007).

3.2.3. Dummy PTO

The model uses a dummy PTO to simulate power generation. This allows for power generation estimates without having to invest in designing complex PTO systems for a relatively early-stage concept. A three-phase brushless DC electric motor has been used as a generator. When there is a resistance load across the motor lead wires, turning the rotor generates an electromagnetic induction force, which causes a torque that opposes said motion. The magnitude of this torque depends on the rotational speed and the value of resistance across the lead

wires. This dummy PTO damping torque is desirable to be linear, as nonlinear damping is much more complicated to model and use in power calculations.

An experiment was conducted to validate that the electric motor exhibited linear damping and to determine the damping coefficients for different resistance loads. The motor being used was a three-phase DC brushless motor with three output leads. A resistor was connected between one of the wires and each of the other two wires, as shown in Fig. 5. The two resistors used were of equal value. Results for a resistance value of 2.8 Ohm are displayed as an example in Fig. 6. This experiment was conducted for all resistance values used in the wave flume experiment (ranging from 1.1 Ohm to 18 Ohm). The rotational speed was measured with a custom-built rotary optical encoder. It can be seen in Fig. 6 that there is a clear linear relationship between the torque and rotational velocity of the motor.

By treating the generator as a dummy PTO system, we are assuming a conversion efficiency of 100%, which of course cannot be true for real generation. In the future, we plan to use an electronic speed controller (ESC) to control the generation, where a lower operating efficiency will occur. The efficiency will also be a function of speed and load. However, as this paper investigates the power potential of the WEC for
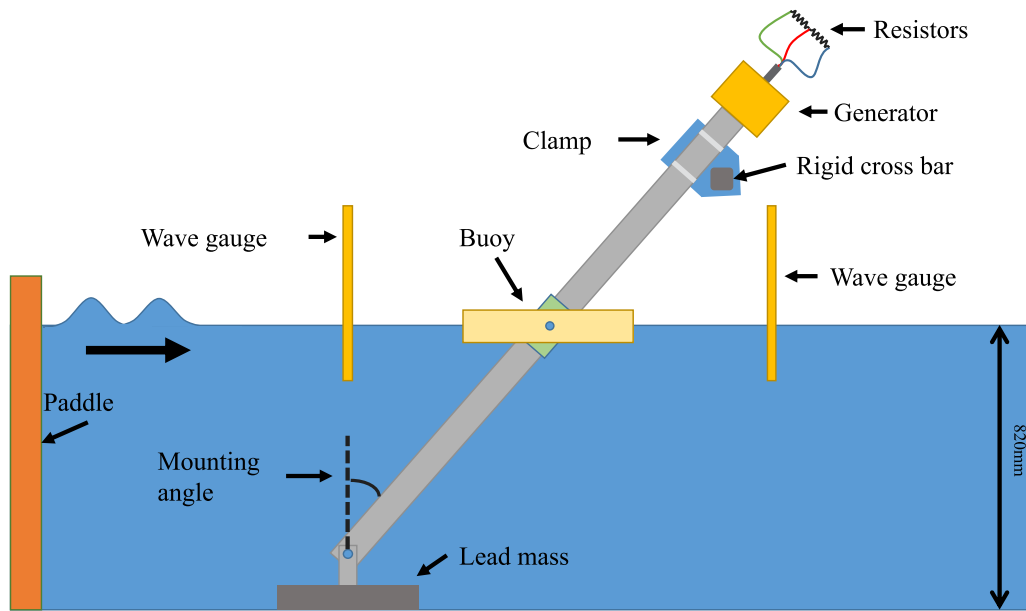
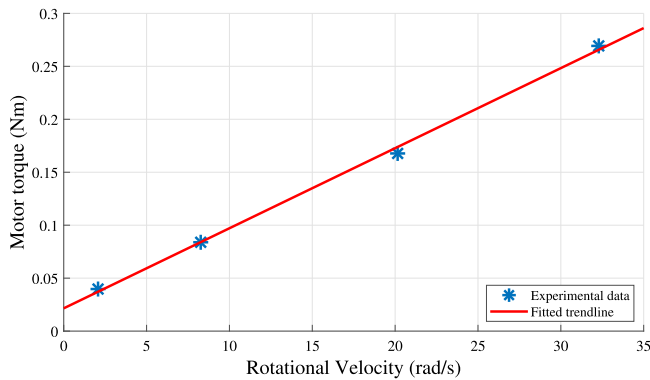Fig. 5. Schematic of the experimental setup in wave flume.

Fig. 6. Torque vs. rotational velocity for resistance value of 2.8 Ohm.

Table 1
The wave parameters for each of the four waves used in the experiment (H is wave height and λ is wavelength; H/λ is wave steepness).

Wave	a	b	c	d
Wave frequency (Hz)	0.3	0.4	0.5	0.6
Wave height (m)	0.31	0.26	0.24	0.23
Water depth (m)	0.82	0.82	0.82	0.82
Wave steepness - H/λ	0.031	0.039	0.053	0.058

different orientations in the water, it is important that the generation efficiency is constant across operating condition to allow for accurate comparisons.

3.2.4. Electrical power calculation

In addition to measuring the dissipated power, the harvested electrical power was also estimated by measuring the voltage across each resistor. The root mean square (RMS) voltage could then be calculated based on the resistor value. The voltage was measured by an Arduino microcontroller. The generator produces both positive and negative voltage values, but the Arduino measures the negative voltages as zero. Therefore, the half-cycle RMS power has been found using Eq. (10). This calculation was done for both resistors across the lead wires, and the two power outputs were added together.

$$P_{RMS} = \sqrt{2 \times \frac{1}{N} \sum_{i=1}^{N} \frac{V_i^2}{R}} \qquad (10)$$

where P_{RMS} is the RMS power, V_i is the instantaneous voltage, R is the resistance value (constant), and N is the total number of data points.

3.2.5. Experimental parameters

The primary objective of the experiment was to determine the conditions under which the model produced the most power. The

main parameters affecting these conditions were the wave frequency, PTO damping coefficient and device mounting angle. Wave frequencies between 0.3 and 0.6 Hz were used, which at 4:1 Froude scaling corresponds to the prevailing wave period of 5–7 s off the north coast of New Zealand (MetOcean New Zealand, 2024; Pickrill and Mitchell, 1979). For each wave frequency, the wave height was selected close to the maximum height the flume could generate for each frequency and water depth. Wave amplitudes higher often spilt water out the back of the flume behind the paddle due to splashing.

Table 1 shows the four sets of wave conditions used in the experiment. For each of the four waves, the WEC was experimentally assessed across six different PTO damping coefficients at four different mounting angles: 0, 15, 30 and 45 degrees. This resulted in a total of 96 experimental runs of two minutes in duration. A settling time of at least three minutes was used between tests to ensure that all reflections had decayed.

3.3. Wave theory

Four different sets of wave conditions are considered experimentally in this paper. Fig. 7 shows coefficients of these wave conditions superimposed over a diagram of the applicability of different wave theories. All four points lie in the intermediate depth wave region, and none are close to the breaking limit due to water depth ($H/h \approx 0.8$) or the breaking limit due to wave steepness ($H/\lambda \approx 0.14$), where H is the wave height, h is the water depth and λ is the wavelength. Three of the four points lie in the Stokes 3rd region. The fourth point lies in the region of 5th-order stream function theory. Matlab scripts based on formulations (Fenton, 1999; Zhao and Liu, 2022) were used to compute the solutions for both Stokes 3rd-order and the 5th-order stream function and thus model the experimentally obtained wave profiles.
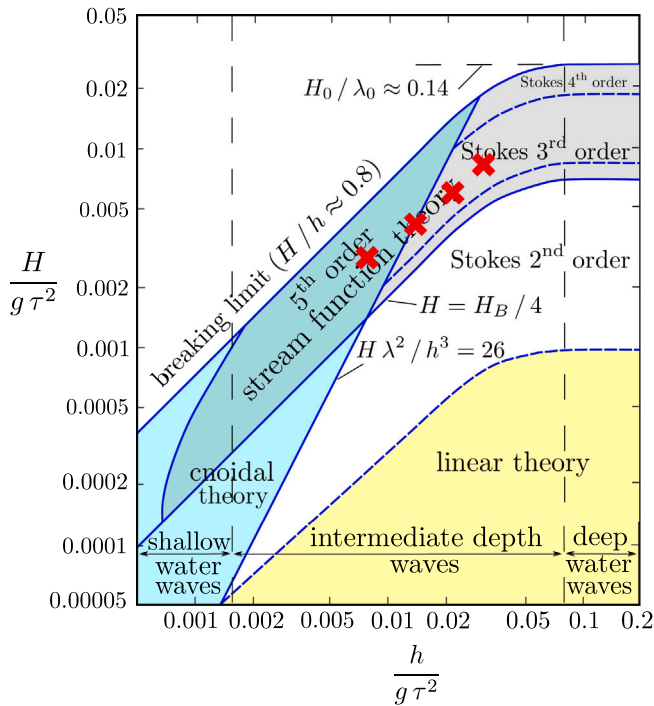
Fig. 7. Wave theory applicability and experimental points (Dean and Dalrymple, 1995).

Wave gauge data from the experiment is compared with Stokes 3rd and 5th-order Stream theory in Fig. 8. Good agreement is seen between the wave gauge data and relevant wave theory models for each frequency, with very similar peak width, frequency and wave height. Some noise can be seen in the wave gauge data, particularly for frequencies 0.3 Hz and 0.5 Hz, which is most likely due to reflections from the wave absorbing parabolic beach at the end of the flume.

4. Results and discussion

4.1. Power output

The experimental and numerical results are plotted on common axes in Fig. 9 to illustrate the WEC performance. For each curve, the power output increased following the approximate trend of a negative quadratic. The power then reaches the quadratic apex before gradually decreasing close to linearly. For each of the four wave frequencies considered, increasing the mounting angle increased the power output, with the 45-degree scenario having a clear advantage. The 30-degree scenario also had a clear advantage over the lower angles. There is no clear or significant difference in power output between mounting angles of 15 and 0 degrees for any frequency.

The benefit in performance for the higher mounting angle is more pronounced for frequencies of 0.4 Hz and 0.5 Hz than for 0.3 Hz and 0.6 Hz. For 0.6 Hz, the 45-degree angle features greater power generation than the other angles, but there is only a 26% increase in the maximum average power compared to the 0-degree scenario. This increase is 50% and 42% for 0.4 Hz and 0.5 Hz respectively. For 0.3 Hz, the power curves are more closely grouped, with the 45-degree angle producing 23% more power than the 0-degree angle at maximum outputs.

After completing the mounting angle experiments, the device was tested in larger waves to achieve higher power using the optimal configuration found in the initial experiment. The results of these larger wave tests are not shown in Fig. 9. The highest average mechanical power output from the experiment was 12.6 W, which occurred for a wave height of 0.32 m, a frequency of 0.4 Hz and a PTO damping coefficient

of 88 Ns m^{-1}. For this case, an average of $6.4 W_{RMS}$ of electrical power was measured, giving an electrical (generator) efficiency of around 50% and a power-to-mass ratio of 1.0 W/kg of moving mass.

4.2. Comparison between experimental and theoretical results

Reasonable agreement is seen between the theoretical and experimental results, both qualitatively and quantitatively. Qualitatively, all experimental datasets and theoretical predictions follow similar patterns, although a few experimental data points vary from these trends. These are likely due to several reasons, including experimental errors and limitations of the numerical model. Quantitatively, the agreement is very good also, especially at mounting angles of 15 and 30 degrees. At 0 and 15 degrees, there are some deviations between the theoretical trendlines and experimental data points, with errors between 5 and 20%.

Some slight variation in wave height occurs between experimental runs. One possible reason for this is slight changes in the flume water depth over time. A control system is in place to keep the water level constant to account for leaks, but it has an accuracy of plus or minus 5 mm. Since the experiment focuses on intermediate depth waves, this small change in depth can result in a change in wave height. One place where with clear variation is for 0 degrees for 0.3 Hz waves. The 0-degree experimental power output data is significantly higher than the numerical predictions in Fig. 9(a). On average, the waves were slightly larger for that group of data, resulting in higher power output.

Experimental results for the 0 and 15-degree scenarios are not obviously distinct from each another, which can be seen in Figs. 9(a)–9(c), unlike the numerical results, where the 15-degree scenario demonstrates higher power output. This is likely due to the minor variations of the incident waves in the experiments. The numerical results do not predict a large difference in power output between the 0 and 15-degree cases, and the expected variation between experimental runs is likely masking this difference in the experimental results.

At the maximum PTO damping coefficient of 213 Ns m^{-1}, the WEC is not operating under its designed conditions, and the motion of the buoy is significantly less than the height of the wave. As such, non-linear effects become more dominant, reducing the numerical model's accuracy. This is especially true for the lower mounting angles, as the motion is noticeably less smooth than for the higher mounting angles. This could be the cause of outliers for PTO damping of 213 Ns m^{-1}, such as the 0-degree points seen in Figs. 9(b) and 9(c), which exceeded the numerical predictions.

Another possible cause of wave height variation is reflections. The wave flume has measures to minimise reflections, such as a perforated parabolic beach and an energy-dissipating wall at the far end. However, some reflections do still occur. Some of these likely come from the end of the flume, but others may be reflecting off the walls, buoy and linear rail itself. This leads to variation in wave height, thus resulting in variation in power output.

The proximity of the flume walls likely has an effect on the performance of the WEC, as the WEC motion will be influenced by reflections from the wall (Chen, 1994). However, single-frequency wave forces can be measured with accuracy so long as the incident and reflected wave frequencies are not similar to the transverse resonant frequency of the wave flume (Chen, 1994). For a water depth of 0.82 m, the fundamental transverse resonant frequency is approximately 0.85 Hz; significantly higher than the frequencies used in the experiments. Additionally, no obvious cross-flume motion can be observed in the footage of the experiment. Therefore, the results for the single wave-frequency experiments are expected to be reasonably accurate.

Fig. 9(d) does not contain data for the 15-degree mounting angle, as the experimental data was compromised. The data did not follow the same trend as the other curves, and on closer inspection of the raw voltage data, it appears that the connection between the generator and one of the resistors had become loose, invalidating the data. The data was therefore removed, and the voltage data was verified for all other experimental runs.
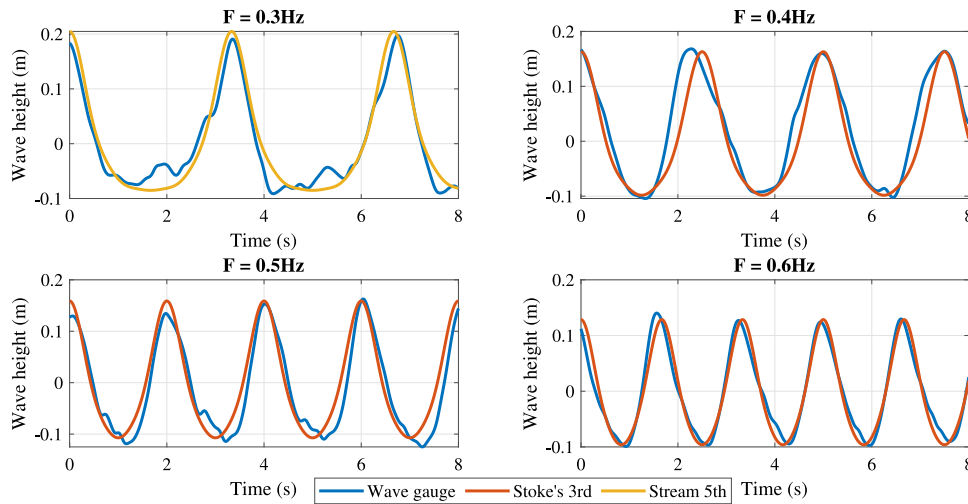
Fig. 8. Wave gauge data compared to wave theories for each of the waves used in the experiment.

4.3. Discussion of the WEC power output

The trend that each mechanical power output vs. PTO damping dataset follows can be explained physically. In the "quadratic" part of the curve, the buoy follows the wave closely, and its motion decreases only slightly with an increase in the PTO damping coefficient. The curve reaches a peak when the PTO damping force becomes close to the maximum buoyancy and weight force of the device. At higher damping coefficients, the damping force is larger than buoyancy and weight forces, and the buoy's motion decreases, and thus, so does the extracted power. In the case of the 45-degree mounting angle, what was apparent from the experiment was that the buoy was never fully submerged when rising, but it did fully emerge when falling. This is because the weight force acting in the direction of motion is smaller than the maximum buoyancy force. This can be seen in Fig. 10, where the buoy rises at the same rate as the wave but clearly lags the wave when falling. Additionally, it can be seen that the amplitude of buoy motion is lower than that of the wave, even though the WEC is mounted at 45 degrees. The PTO damping force is great enough to significantly decrease the buoy's motion in these wave conditions.

Consider Fig. 11, which displays the velocity factor coefficient, defined in Eq. (11).

$$C_{vel} = \frac{\max(w)}{\max(\dot{z})} \tag{11}$$

where w is the maximum wave vertical velocity and $\dot{z}$ is the buoy's maximum vertical velocity. Note that the velocity factor is not a conventional performance measure but has instead been defined for illustrative purposes.

The maximum wave and buoy velocities have been calculated using numerical differentiation of the experimental data. Only the vertical component of motion is considered for simplicity and comparability. C_{vel} can be calculated separately for when the buoy is rising and when the buoy is falling. Fig. 11 shows the velocity factor against the PTO damping coefficient for two different mounting angles. The upwards and downwards velocity factors are given. At low damping coefficients, the downwards velocity factor is close to 1, while the upwards velocity factor is lower. As PTO damping increases, the downward velocity factor drops significantly, particularly at the higher mounting angle. The upward velocity factor decreases as well, though not as steeply.

To tune the WEC to move more smoothly in the waves, the PTO damping force should be lower when the device is falling than rising so that the device can closely follow the wave, possibly also resulting in increased power generation. Alternatively, the density of the buoy could be increased to increase the gravity force without changing the buoyancy. However, this would increase the amount of material used and may not be the most cost-effective solution. Planned future work includes investigating both of these options to determine whether additional power can be generated.

4.4. Modelling increased scale WEC device

The Simulink model was used to estimate how a scaled-up WEC will perform in real ocean conditions. One possible location to test the device is off the north coast of New Zealand, where the prevailing wave height is 0.5–1.5 m and the prevailing wave period is 5–7 s (MetOcean New Zealand, 2024; Pickrill and Mitchell, 1979).

The numerical model was adapted to model the conditions of the proposed ocean test. The selected wave conditions were a wave of 1.0 m in height with a period of 5 s and a water depth of 4.0 m; realistic nearshore conditions off the North coast of New Zealand. Using a scaling factor of 2:1, the mass of the buoy was increased to 50 kg. The hydrodynamic coefficients were scaled based on the increased mass and decreased frequency, and the drag force coefficient was scaled by the increased surface area. These conditions lie in the applicability region of Stokes 3rd wave theory, so Stokes 3rd solutions were used in the model.

Fig. 12(a) shows the predicted performance of the device, with a predicted maximum time-average mechanical power output of 125 W. It is assumed that the device will behave qualitatively similar to what was observed in the wave flume. It will most likely be mounted to a large aquafarming structure, and it is assumed that this structure will be bottom fixed or large enough to resist the motion of the waves and provide enough rigidity for the WEC to mount to Stevens et al. (2007), although the detailed design of the mounting system is outside the scope of this project.
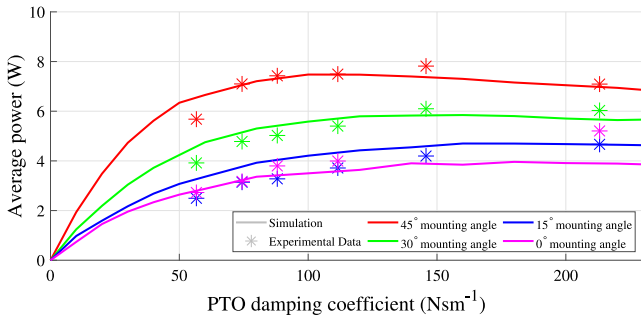
A scaling factor of 4:1 was also used, with the results displayed in Fig. 12(b). With the same wave conditions and a 400 kg buoy mass, the maximum predicted time-average mechanical power is around 1150 W. It is unlikely that a WEC of this size could mount to an existing floating aquafarming structure, so it would attach to a fixed structure or the sea bed.
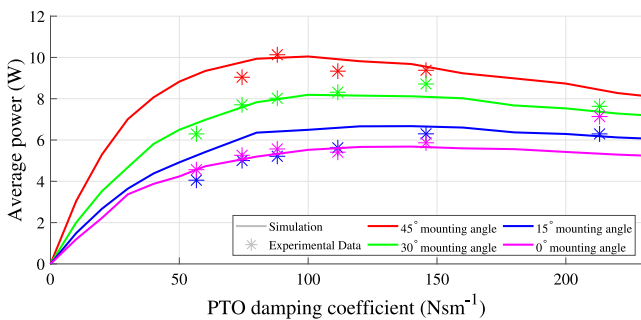
5. Conclusions

In this study, a point absorber WEC has been proposed, then analysed theoretically and experimentally. The device harnesses energy from the linear motion of a floating buoy along a rail, using a specifically designed magnetic mechanism to convert this motion into high-speed rotation of a generator. The WEC was analysed numerically using
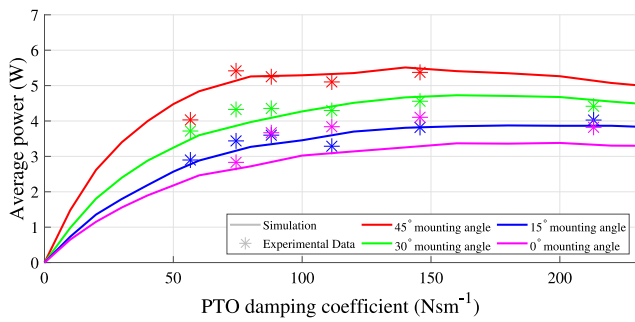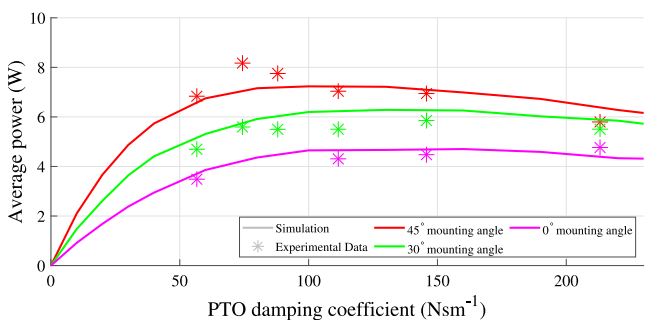
(a) f = 0.3Hz and H = 0.31m

(b) f = 0.4Hz and H = 0.26m

(c) f = 0.5Hz and H = 0.24m

(d) f = 0.6Hz and H = 0.23m

Fig. 9. Simulated and experimental dependencies of the average mechanical power output on the PTO damping coefficient for varying WEC mounting angle, wave height H, and frequency f.
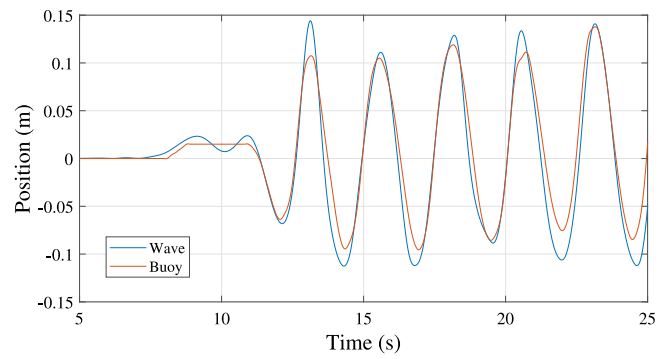

Fig. 10. Wave height and buoy position over time for a 45-degree mounting angle at a high PTO damping.
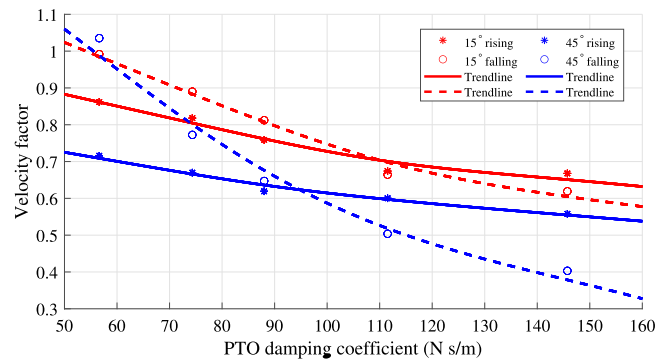

Fig. 11. Velocity factor of the buoy at two different mounting angles, with a wave frequency of 0.3 Hz.

1. The mounting angle has a significant impact on WEC power generation. The experimental results demonstrate that increasing the mounting angle to 45 degrees can lead to a substantial increase in power output. Specifically, the device exhibited up to a 50% increase in power compared to a 0-degree angle, with an average improvement of 35% across tested frequencies.

2. The experimental model, featuring a 6.4 kg moving mass, achieved a maximum average mechanical power output of 12.6 W. With an electrical efficiency of approximately 50%, the harvested electrical power was measured at 6.4 W. This results in a performance metric of 1.0 W/kg of moving mass, which is competitive with leading wave energy converters.

3. The findings from this study contribute valuable insights to the field of wave energy conversion. By achieving comparable performance metrics to cutting-edge WECs, the proposed design showcases promising potential for practical applications in renewable energy production.

6. Future work

In moving forward with this research, there are several key areas where current limitations can be addressed and power output can be further optimised as follows.

1. Increasing the mounting angle beyond 45 degrees is likely to result in further increases in power output. Future work could include modifications to the buoy geometry to allow higher mounting angles to be implemented.

2. A control system could be implemented to control the PTO damping coefficient in situ and adjust the value for the case when the buoy is rising versus when it is falling.
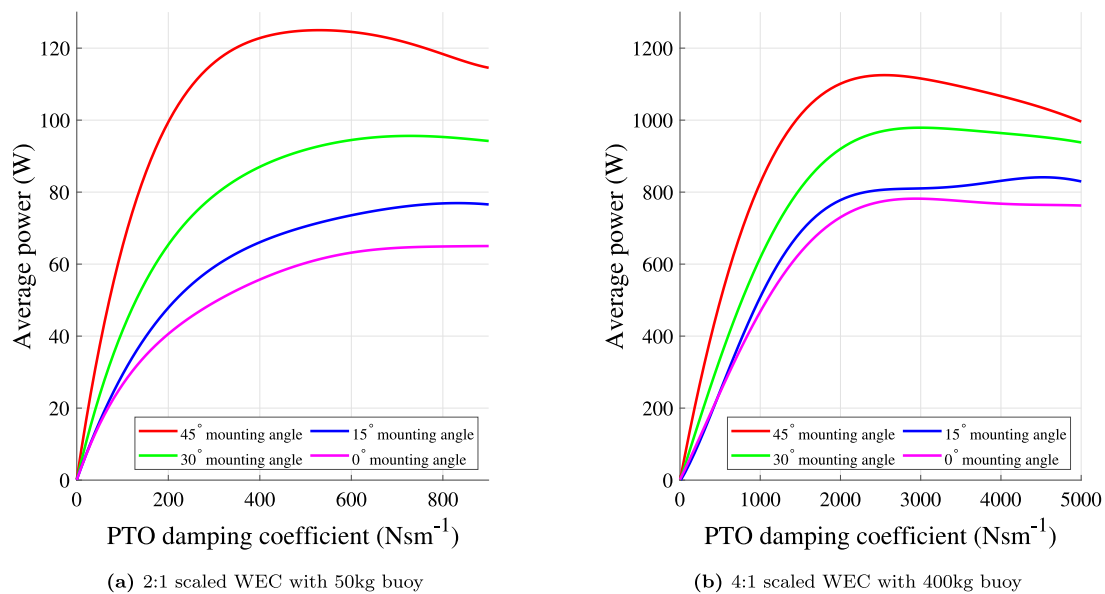
a time-domain model in Simulink, and experimentally in the UoA wave flume. The results of these analyses are compared, and projections for larger-scale devices are given. The concluding remarks are summarised below.

(a) 2:1 scaled WEC with 50kg buoy

(b) 4:1 scaled WEC with 400kg buoy

Fig. 12. Numerical prediction for scaled WEC in ocean waves with a height of 1.0 m and period of 5 s.

3. Wave flume testing with more realistic sea-states could be conducted to provide further confidence in the full-scale modelling predictions, including the variation of significant wave height and spectral shape. Different wave directions relative to the WEC could also be considered to assess its performance under various wave directions.

CRediT authorship contribution statement

Jonathan Everett: Writing – original draft, Methodology, Investigation, Conceptualization. **Vladislav Sorokin:** Writing – review & editing, Supervision. **Colin Whittaker:** Writing – review & editing, Supervision. **Kean Aw:** Writing – review & editing, Supervision.

Declaration of competing interest

The authors declare that they have no known competing financial interests or personal relationships that could have appeared to influence the work reported in this paper.

Data availability

Data will be made available on request.

Acknowledgements

References

Brown, W.S., 2016. Elements of physical oceanography. In: Dhanak, M.R., Xiros, N.I. (Eds.), Springer Handbook of Ocean Engineering. Springer International Publishing, Cham, pp. 15–46. http://dx.doi.org/10.1007/978-3-319-16649-0_2.

Cai, Y., Huo, Y., Shi, X., Liu, Y., 2022. Numerical and experimental research on a resonance-based wave energy converter. Energy Convers. Manage. 269, 116–152. http://dx.doi.org/10.1016/j.enconman.2022.116152.

Chen, X., 1994. On the side wall effects upon bodies of arbitrary geometry in wave tanks. Appl. Ocean Res. 16 (6), 337–345. http://dx.doi.org/10.1016/0141-1187(94)00017-4, https://www.sciencedirect.com/science/article/pii/0141118794000174.

Clemente, D., Rosa-Santos, P., Ferradosa, T., Taveira-Pinto, F., 2023. Wave energy conversion energizing offshore aquaculture: Prospects along the Portuguese coastline. Renew. Energy 204, 347–358. http://dx.doi.org/10.1016/j.renene.2023.01.009, https://www.sciencedirect.com/science/article/pii/S0960148123000095.

CorPower, 2023. Wave energy technology. (Retrieved 19 April 2024), from https://corpowerocean.com/wave-energy-technology/.

Dean, R.G., Dalrymple, R.A., 1995. Nonlinear waves. In: Water Wave Mechanics for Engineers and Scientists. World Scientific, pp. 295–325.

Ermakov, A., Ringwood, J.V., 2021. Rotors for wave energy conversion—Practice and possibilities. IET Renew. Power Gener. 15 (14), 3091–3108. http://dx.doi.org/10.1049/rpg2.12192, https://ietresearch.onlinelibrary.wiley.com/doi/abs/10.1049/rpg2.12192.

Evans, D., Jeffrey, D., Salter, S., Taylor, J., 1979. Submerged cylinder wave energy device: theory and experiment. Appl. Ocean Res. 1 (1), 3–12. http://dx.doi.org/10.1016/0141-1187(79)90003-8, https://www.sciencedirect.com/science/article/pii/0141118779900038.

Fenton, J.D., 1999. Numerical methods for nonlinear waves. Adv. Coast. Ocean Eng. 241–324. http://dx.doi.org/10.1142/9789812797544_0005.

Folley, M., Whittaker, T., 2009. Analysis of the nearshore wave energy resource. Renew. Energy 34 (7), 1709–1715. http://dx.doi.org/10.1016/j.renene.2009.01.003, https://www.sciencedirect.com/science/article/pii/S0960148109000160.

Folley, M., Whittaker, T., Henry, A., 2007. The effect of water depth on the performance of a small surging wave energy converter. Ocean Eng. 34 (8), 1265–1274. http://dx.doi.org/10.1016/j.oceaneng.2006.05.015, https://www.sciencedirect.com/science/article/pii/S0029801806001892.

Freeman, M., Garavelli, L., Wilson, E., Hemer, M., Abundo, M., Travis, L., 2022. Offshore aquaculture: a market for ocean renewable energy. Report for ocean energy systems (OES).

Giassi, M., Thomas, S., Tosdevin, T., Engström, J., Hann, M., Isberg, J., Göteman, M., 2020. Capturing the experimental behaviour of a point-absorber WEC by simplified numerical models. J. Fluids Struct. 99, 103–143. http://dx.doi.org/10.1016/j.jfluidstructs.2020.103143, https://www.sciencedirect.com/science/article/pii/S0889974620306125.

Hamilton, A., 2016. Buoy technology. In: Dhanak, M.R., Xiros, N.I. (Eds.), Springer Handbook of Ocean Engineering. Springer International Publishing, Cham, pp. 937–962. http://dx.doi.org/10.1007/978-3-319-16649-0_40.

Jiang, B., Li, X., Chen, S., Xiong, Q., Chen, B.-f., Parker, R.G., Zuo, L., 2020. Performance analysis and tank test validation of a hybrid ocean wave-current energy converter with a single power takeoff. Energy Convers. Manage. 224, 113–268. http://dx.doi.org/10.1016/j.enconman.2020.113268.

Li, M., Jing, X., 2021. A bistable X-structured electromagnetic wave energy converter with a novel mechanical-motion-rectifier: Design, analysis, and experimental tests. Energy Convers. Manage. 244, 114–466. http://dx.doi.org/10.1016/j.enconman.2021.114466.

Lopez, I., Andreu, J., Ceballos, S., Martínez de Alegría, I., Kortabarria, I., 2013. Review of wave energy technologies and the necessary power-equipment. Renew. Sustain. Energy Rev. 27, 413–434. http://dx.doi.org/10.1016/j.rser.2013.07.009.

MetOcean New Zealand, 2024. (Retrieved 19 April 2024), from https://insights.metservice.com/hindcast/#/.

Negri, M., Malavasi, S., 2022. Laboratory testing of a combined heaving-surging wave energy converter for the Nearshore Zone. Ocean Eng. 244, 110–421. http://dx.doi.org/10.1016/j.oceaneng.2021.110421.

Newman, J., 1977. Marine Hydrodynamics. Wei Cheng Cultural Enteroprise Company, https://books.google.co.nz/books?id=nj-k_lAmaBYC.

Ocean Harvesting, 2023. Technology - ocean harvesting. (Retrieved 19 April 2024), from https://oceanharvesting.com/our-technology/.

Ocean Power Technologies, 2024. PB3 PowerBuoy. (Retrieved 19 April 2024), from https://oceanpowertechnologies.com/platform/opt-pb3-powerbuoy/.

Pecher, A., Kofoed, J.P., Larsen, T., 2012. Design specifications for the hanstholm WEPTOS wave energy converter. Energies 5 (4), 1001–1017. http://dx.doi.org/10.3390/en5041001, https://www.mdpi.com/1996-1073/5/4/1001.

Pickrill, R.A., Mitchell, J.S., 1979. Ocean wave characteristics around New Zealand. New Zealand J. Mar. Freshw. Res. 13 (4), 501–520. http://dx.doi.org/10.1080/00288330.1979.9515827.

Salter, S., 1980. Recent progress on ducks. IEE Proc. A Phys. Sci. Meas. Instrum. Manag. Educ. Rev. 127 (5), 308. http://dx.doi.org/10.1049/ip-a-1.1980.0049.

Steffen, L., 2022. The waveline magnet offers the cheapest clean energy ever. (Retrieved 19 April 2024), from https://www.intelligentliving.co/waveline-magnet-cheapest-clean-energy-ever/.

Stevens, C.L., Plew, D.R., Smith, M.J., Fredriksson, D.W., 2007. Hydrodynamic forcing of long-line mussel farms: Observations. J. Waterw. Port Coast. Ocean Eng. 133 (3), 192–199. http://dx.doi.org/10.1061/(asce)0733-950x(2007)133:3(192).

Swel, 2024. Research - swel. (Retrieved 19 April 2024), from https://swel.eu/research/.

TETHYS, 2018. Wave dragon pre-commercial demonstration project. (Retrieved 19 April 2024), from https://tethys.pnnl.gov/project-sites/wave-dragon-pre-commercial-demonstration-project.

TETHYS, 2020. Wello penguin at EMEC. (Retrieved 19 April 2024), from https://tethys.pnnl.gov/project-sites/wello-penguin-emec.

The New Zealand Government, 2019. Aquaculture strategy. https://www.mpi.govt.nz/fishing-aquaculture/aquaculture-fish-and-shellfish-farming/aquaculture-strategy-for-new-zealand/.

USDOE, 2019. Powering the blue economy: Exploring opportunities for marine renewable energy in maritime markets. (Retrieved 19 April 2024), from https://www.energy.gov/sites/default/files/2019/09/f66/73355-4.pdf.

WaveSwell, 2023. https://www.waveswell.com/.

WEC-sim, 2022. Theory manual. (Retrieved 19 April 2024), from https://wec-sim.github.io/WEC-Sim/master/theory/index.html.

Yue, W., Wang, Z., Ding, W., Sheng, S., Zhang, Y., Huang, Z., Wang, W., 2023. Feasibility of co-locating wave energy converters with offshore aquaculture: The pioneering case study of China's Penghu platform. Ocean Eng. 288, 116039. http://dx.doi.org/10.1016/j.oceaneng.2023.116039, https://www.sciencedirect.com/science/article/pii/S002980182302423X.

Yurchenko, D., Alevras, P., 2018. Parametric pendulum based wave energy converter. Mech. Syst. Signal Process. 99, 504–515. http://dx.doi.org/10.1016/j.ymssp.2017.06.026, https://www.sciencedirect.com/science/article/pii/S0888327017303382.

Zhao, K., Liu, P.L.-F., 2022. On Stokes wave solutions. Proc. R. Soc. Lond. Ser. A Math. Phys. Eng. Sci. 478 (2258), http://dx.doi.org/10.1098/rspa.2021.0732.